

Cite this: DOI: 10.1039/xxxxxxxxxx

Comparison of Classical Reaction Paths and Tunneling Paths studied with the Semiclassical Instanton Theory[†]

Jan Meisner,^a Max N. Markmeyer,^a Matthias U. Böhner,^a and Johannes Kästner^{*a}

Received Date

Accepted Date

DOI: 10.1039/xxxxxxxxxx

www.rsc.org/journalname

Atom tunneling in the hydrogen atom transfer reaction of the 2,4,6-tri-*tert*-butylphenyl radical to 3,5-di-*tert*-butylneophyl, which has a short but strongly curved reaction path, was investigated using instanton theory. We found the tunneling path to deviate qualitatively from the classical intrinsic reaction coordinate, the steepest-descent path in mass-weighted Cartesian coordinates. To perform that comparison, we implemented a new variant of the predictor-corrector algorithm for the calculation of the intrinsic reaction coordinate. We used the reaction force analysis method as a mean to decompose the reaction barrier into structural and electronic components structural and electronic components. Due to the narrow energy barrier atom tunneling is important in the abovementioned reaction, even above room temperature. Our calculated rate constants between 350 K and 100 K agree well with experimental values. We found a H/D kinetic isotope effect of almost 10^6 at 100 K. Tunneling dominates the protium transfer below 400 K and the deuterium transfer below 300 K. We compared the lengths of the tunneling path and the classical path for the hydrogen atom transfer in the reaction $\text{HCl} + \text{Cl}$ and quantified the corner cutting in this reaction. At low temperature, the tunneling path is about 40% shorter than the classical path.

1 Introduction

Atom tunneling plays an important role in chemistry as it enhances the reaction rate constants of chemical reactions. At very low temperatures it determines stability and reactivity.^{1–3} The tunneling of atoms, in particular hydrogen atoms, is important in different fields of chemistry ranging from biochemistry^{4–6} to astrochemistry.^{7,8} Several reviews about atom tunneling were published recently.^{9–12}

There are many methods to compute the effect of atom tunneling on the rate constants of chemical reactions.^{10,13,14} In principle, a full quantum mechanical description of the nuclear wave function is a fully rigorous treatment.^{15,16} These methods require the solution of the time-dependent Schrödinger equation, which poses huge computational demands if the problem exceeds a few atoms.

A much simpler approach of including the quantum mechanical tunneling effect is to use classical rate constants and correct them by tunneling through approximate potential functions for which

the tunneling probability can be calculated analytically. The most prominent of these approaches use rectangular barriers, parabolic barriers¹⁷ or Eckart barriers.¹⁸ These approaches assume the tunneling particles to take the same path as particles crossing the potential energy barrier classically. They are sometimes referred to as one-dimensional tunneling corrections.

The tunneling probability, however, is increased by shortening the tunneling path. While the average classical path, *i.e.*, the minimum energy path (MEP), proceeds through a first-order saddle point on the potential energy surface (PES), the transition structure (TS), the tunnelling path cuts the corner on the concave side of curved reaction paths on the expense of higher potential energy.^{19–21} Methods which take this into account are sometimes termed multidimensional tunneling corrections, like the small curvature tunneling correction (SCT).²² Such methods still rely on the classical MEP as a reference for the tunneling path of the particles.

In this work we use the semiclassical instanton theory^{23–38} based on Feynman's path integral formalism.³⁹ At temperatures below the crossover temperature

$$T_c = \frac{\hbar\omega_{TS}}{2\pi k_B} \quad (1)$$

atom tunneling dominates the reaction rate and instanton theory is applicable. The underlying idea is to optimize a tunneling path,

^a Institute for Theoretical Chemistry, University of Stuttgart, Pfaffenwaldring 55, Stuttgart, Germany. Fax: +49-(0)711-685 64442; Tel: +49-(0)711-685 64473; E-mail: kaestner@theochem.uni-stuttgart.de

[†] Electronic Supplementary Information (ESI) available: Full description of the implemented algorithm, results of the functional benchmark, and reaction rate constants. See DOI: 10.1039/b000000x/

the instanton, for each temperature by making the Euclidean action stationary. Instanton theory has become a useful method to study reactions and is nowadays an established approach to calculate rate constants in different fields of chemistry.^{11,40–66} The instanton is particularly advantageous when the tunneling path qualitatively deviates from the classical path for example at very low temperatures.^{61,67} In these cases instanton theory was found to be superior to MEP based methodologies like SCT.⁴⁷

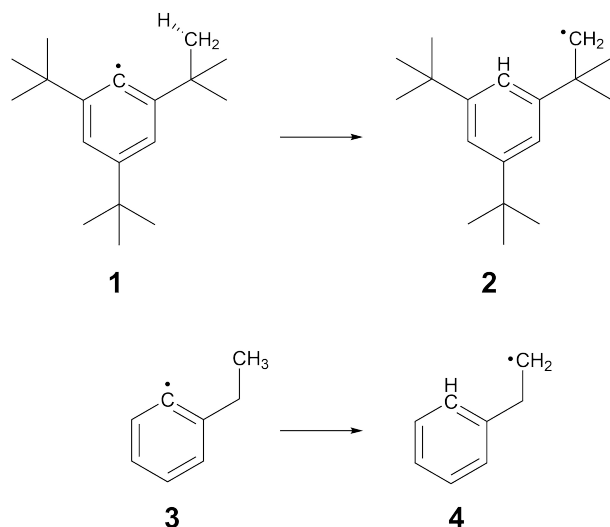


Fig. 1 Reactions discussed in this study.

The isomerization of aryl radicals as described by Brunton *et al.*⁶⁸ is one example of hydrogen atom transfer reactions where atom tunneling has a pronounced effect on the reactivity. Brunton *et al.* studied various rate constants by means of electron paramagnetic resonance spectroscopy pointing out that quantum mechanical tunneling is the reason for the strong non-Arrhenius behavior.⁶⁸ The isomerization of the 2,4,6-tri-*tert*-butylphenyl radical (1) to the 3,5-di-*tert*-butylneophyl radical (2), see Fig. 1, was studied from 113 K to 247 K. The authors also performed experiments where they substituted all methyl hydrogen atoms by deuterium, which is here referred to as the perdeuterated system. For that, rate constants from 123 K to 293 K were measured. At the lowest temperatures studied, Brunton *et al.* found a H/D kinetic isotope effect (KIE) larger than four orders of magnitude due to atom tunneling.⁶⁸

In this paper we study the reaction $1 \rightarrow 2$ using instanton theory. Particular emphasis is put on the reaction path with and without tunneling. The most likely classical reaction path is the intrinsic reaction coordinate (IRC), which is the mass-weighted MEP in Cartesian coordinates. To compare the IRC to the instanton path, we implemented IRC search algorithms in our DL-FIND code.⁶⁹ We present a modified version of the Hessian predictor-corrector (HPC) algorithm by Hratchian *et al.*^{70,71} to determine IRCs. Besides $1 \rightarrow 2$, we use the reaction $\text{HCl} + \text{Cl}$ to compare the lengths of the classical reaction path and instanton tunneling paths.

2 Methods

2.1 Intrinsic Reaction Coordinate

The IRC connects the reactant's and product's minima and allows insight into the mechanism of chemical reactions. It is defined as the steepest descent MEP in mass-weighted Cartesian coordinates \mathbf{x} .⁷² The evaluation of the IRC begins at a saddle point of first order, the transition structure, and follows the negative of $\mathbf{g}(\mathbf{x})$, the gradient of the multidimensional PES:

$$\frac{d\mathbf{x}}{ds} = -\frac{\mathbf{g}(\mathbf{x})}{|\mathbf{g}(\mathbf{x})|} \quad (2)$$

Here s is the arc length along the MEP in mass-weighted Cartesian coordinates.

We implemented a variant of the well-established Hessian predictor-corrector (HPC) method by Hratchian *et al.*⁷⁰ In summary, the idea is to use a fast integration method (here we use the explicit Euler integration) as a first estimation, the so-called predictor step. After that, a more sophisticated method is used to improve this first estimation, called corrector step. In the HPC integrator, the latter is determined by means of a modified Bulirsch–Stoer (mBS) integrator as described by Hratchian *et al.*⁷⁰ The original Bulirsch–Stoer algorithm is described well elsewhere.⁷³

For the predictor step, the original HPC approach⁷⁰ solves the integration of equation (2) analytically, which is possible when using local quadratic approximation (LQA).^{74,75} This requires a matrix diagonalization rendering the treatment of bigger systems difficult.⁷⁶ To avoid the diagonalization, the predictor step of the HPC was changed to a plain explicit Euler integration resulting in the Euler-predictor-corrector (EulerPC) presented by Hratchian *et al.*:^{76,77}

$$\mathbf{x}_{i+1}^{[P]} = \mathbf{x}_i - \Delta s \frac{\mathbf{g}(\mathbf{x}_i)}{|\mathbf{g}(\mathbf{x}_i)|} \quad (3)$$

In our implementation, we build a Taylor series up to quadratic order, *i.e.*, including the Hessian matrix and use the simple explicit Euler method for the predictor step to avoid the matrix diagonalization, yet improving the quality of the predictor step by incorporation of quadratic information.

Other aspects of the HPC were treated as described in the literature.⁷⁰ The full description of the technical implementation into DL-Find including the first step and termination is sketched in the Supplementary Information.

2.2 Computational Details

To give reliable rate constants, the underlying electronic potential has to be accurate. Wave-function-based correlation methods like CCSD(T)-F12 provide a good solution of the electronic Schrödinger equation but are not suitable for the direct use in our study because of their computational effort, especially for the calculation of gradients and Hessians of the potential energy, as required by instanton theory. Therefore, and because of the large number of function evaluations necessary for the optimization of stationary points and IRCs on the PES as well as instantons, we decided to use density functional theory (DFT). Finding a functional which describes the reaction adequately in comparison to reliable correlation methods was still too costly in this case.

Therefore we used a reduced model, namely the isomerization of phenylethyl radical **3** to ethylenebenzene radical **4**. This reaction is very similar to the reaction of **1** to **2** and can serve as a benchmark.

Initially, geometries were optimized using the B3LYP density functional^{78–83} and the def2-SVP⁸⁴ basis set. On these geometries, energies were computed using explicitly correlated unrestricted coupled-cluster with singles and doubles excitations including perturbative treatment of triple excitations (CCSD(T)-F12)^{85,86} based on a restricted Hartree–Fock (RHF) reference function and the cc-pVTZ-F12⁸⁷ basis set. The two relevant energy differences – the electronic activation energy E_A and the electronic reaction energy ΔE were then compared to the corresponding values obtained by single point energy calculations with different functional/basis set combinations. For that, we applied commonly used density functionals (B3LYP^{78–83} PBE^{78,79,88,89} PBE0^{78,79,88–90} BP-86^{78–81,91} B3LYP,^{78–82,92} TPSS^{78,79,88,93} TPSSH^{78,79,88,93,94} M06⁹⁵) and the basis sets def2-SVP⁸⁴, def2-TZVP⁸⁴, and def2-TZVPD⁹⁶. We also tested the influence of a D3 dispersion correction.⁹⁷

The CCSD(T)-F12 calculations were carried out in Molpro⁹⁸ version 2012.1 with the cc-pVTZ-F12⁸⁷ basis set.

DFT energies, gradients and second derivatives were calculated in the Turbomole program package version 7.0.1.⁹⁹ SCF energies were iterated until the energy of two successive iterations changes by less than $1.0 \cdot 10^{-9}$ a.u. on the $m5$ multigrid.¹⁰⁰ First and second derivatives with respect to the nuclear coordinates (gradients and Hessians) are calculated analytically.

All geometry optimizations, IRCs, instantons and rate constants have been calculated with DL-Find⁶⁹ interfaced to ChemShell.^{101,102} The IRC path is calculated with a step size of $\Delta s = 0.04$ mass-weighted atomic units. Hessian updates according to Bofill's formula¹⁰³ were used throughout the whole calculation of the IRC.⁷¹ Stationary points were identified based on the number of imaginary frequencies: zero for minimum structures and exactly one for the transition structures.

Instantons and rate constants were calculated using sequential cooling: the instanton at a particular temperature is used as a starting guess for the next lower temperature and the Hessians are used for a quasi-Newton–Raphson optimizer.^{53,54} The Feynman path was discretized to 40 images down to 214 K and to 78 images down to 100 K. The convergence with respect to the number of images was shown by an additional instanton calculation using 154 images at 100 K where the rate constant deviated by less than 0.2 % from the rate constants obtained with 78 images. All coordinates (135 degrees of freedom in case of **1** → **2**) were optimized during the instanton search until the maximum component of the gradient was less than $1.0 \cdot 10^{-8}$ a.u. (1 a.u. = $a_0 \sqrt{m_e}$).

For the reaction HCl + Cl we are interested in the shape of the classical reaction path compared to instanton paths. For that we have chosen the B3LYP functional^{78–83} and the def2-SVP basis set⁸⁴ due to their computational efficiency and assume that geometries, reaction paths, and instantons are reasonably represented.

3 Results

In this section we describe the electronic potential energy of the isomerization of **1** to **2** including a benchmark of the different density functionals using the reduced model reaction **3** → **4**. Following that, the IRC of the reaction obtained with the newly implemented algorithm is discussed. We present rate constants, compare them to literature data,⁶⁸ and analyze the tunneling path. Finally, we discuss the reaction of HCl + Cl and quantify the corner cutting effect.

3.1 Electronic Structure

Eight commonly used density functionals with and without D3 correction for dispersion were tested against CCSD(T)-F12/cc-pVTZ-F12 energies on B3LYP/def2-SVP geometries. CCSD(T) is sometimes referred to as the gold standard of quantum chemistry as long as the electronic structure of the studied molecule can be expected to be a single reference case. The explicitly correlated variant of it, named CCSD(T)-F12, improves the basis set convergence of the electronic energy such that a triple- ζ basis can be assumed to be sufficiently close to the basis set limit due to improved convergence of the correlation energy.^{85,86}

A legitimation for the assumption that the reaction has just minor multireference character is given by the T1 and D1 diagnostics which are T1 = 0.013 and D1 = 0.043 for the reactant, T1 = 0.011 and D1 = 0.030 for the product, and T1 = 0.012 and D1 = 0.030 for the TS. They are thus below the threshold of T1 = 0.045 and D1 = 0.050 for open shell systems.^{104,105}

The CCSD(T)-F12 calculations resulted in an electronic activation energy of $E_A = 86.72$ kJ mol^{−1} and a electronic reaction energy of $\Delta E = -41.46$ kJ mol^{−1}.

The numerical results of the functional benchmark are shown in the Supplementary Information. For the accurate calculation of rate constants, the region around the transition structure is most important, *i.e.*, the electronic energy barrier E_A has to fit the reference CCSD(T)-F12 values. The B3LYP-D3 method provides the smallest deviation and underestimates the barrier by just 3.43 kJ mol^{−1}. Almost all functionals describe the electronic reaction energy ΔE nicely, nearly independently of the basis set. The error of 2.35 kJ mol^{−1} for the electronic reaction energy of the B3LYP-D3/def2-TZVP combination is acceptable. For this reaction, there is no need for diffuse functions as for all functionals, the error introduced by neglecting them is smaller than 1 kJ mol^{−1}. Overall we have chosen the B3LYP functional with the D3 dispersion correction and the def2-TZVP basis set as an appropriate method leading to a reliable electronic potential for the reaction of **3** to **4** and we assume that the reaction **1** → **2** is also well described by this method.

3.2 Intrinsic Reaction Coordinate

Using B3LYP-D3/def2-TZVP the electronic activation energy is $E_A = 78.9$ kJ mol^{−1} and the electronic reaction energy is $\Delta E = -31.6$ kJ mol^{−1}. Inclusion of the harmonically approximated vibrational zero-point energy (ZPE) changes these numbers slightly to $E_{A,ZPE} = 64.0$ kJ mol^{−1} and $\Delta E_{ZPE} = -35.8$ kJ mol^{−1}. The imag-

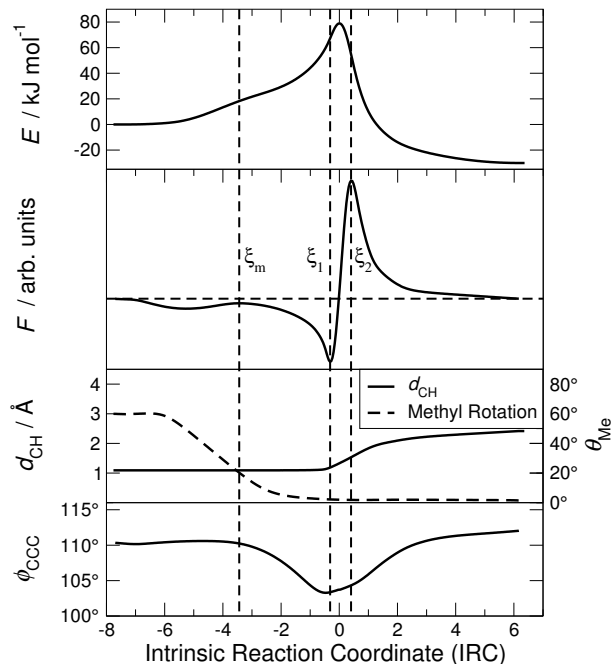


Fig. 2 Geometrical and energetical characterization of the progress from 1 to 2. The vertical dashed lines correspond to the characteristic points of the reaction force mentioned in the text. First graph: Potential energy along the IRC for the hydrogen transfer reaction of 1 → 2. Second graph: Reaction force F during the reaction. The two lowest graphs show the bond distance d_{CH} of the broken C–H bond and θ_{Me} , the angle of the methyl rotation and ϕ_{CCC} , the C–C–C angle of three of the carbon atoms involved in the five-membered ring in the transition structure, respectively.

inary frequency at the transition structure is $1811i \text{ cm}^{-1}$ which leads to a crossover temperature of $T_c = 414 \text{ K}$.

During the reaction, the hydrogen atom migrates from a tert-butyl group to the phenyl ring to form a C–H- σ bond with the aryl carbon atom. Thermodynamically, the reaction is favored because of the high instability of the aryl radical 1. During the reaction and in particular at the TS, the two carbon atoms of the tert-butyl group, two carbon atoms of the phenyl ring, and the transferred hydrogen atom form a planar five-membered ring which reduces the distance the hydrogen atom has to cover.⁶⁸

We calculated the IRC and the corresponding potential energy, see Fig. 2. In the direct vicinity of the TS, the curvature of the potential energy along the barrier is astonishingly high. Note that

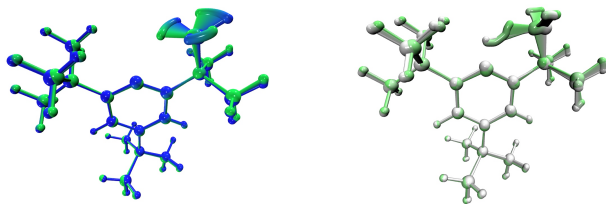


Fig. 3 Geometrical representation of the IRC. The IRC can be split into two parts: the rotation of the methyl group (in the left picture from blue (1) to green) and the C–H bond breaking (in the right picture from green to white (2)).

the distance in mass-weighted Cartesian coordinates is very short. This is also shown by the high absolute value of the imaginary frequency of 1811 cm^{-1} . On the product side of the reaction profile, the system directly proceeds down the potential energy surface towards the product structure. On the reactant side of the barrier, the gradient of the potential energy with respect to the IRC diminishes and a shoulder arises in the plot of the potential energy against the reaction coordinate as visible in the top graph in Fig. 2.

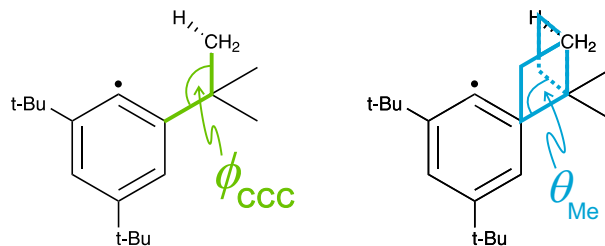


Fig. 4 Definition of the angles ϕ_{CCC} (left) and θ_{Me} (right) in 1.

To study the progress of the reaction along the IRC we concentrated on three internal coordinates, while all degrees of freedom were included in the IRC search: d_{CH} , the distance of the C–H bond to be broken during the reaction, θ_{Me} , a C–C–H torsion angle describing the rotation of the methyl group losing the hydrogen atom around the aliphatic C–C bond, and ϕ_{CCC} , the angle of three carbon atoms involved in the five-membered ring of the transition structure. The two angles are indicated in Fig. 4. In the reactant 1 these are $d_{\text{CH}} = 1.092 \text{ Å}$, $\theta_{\text{Me}} \approx 60.0^\circ$, and $\phi_{\text{CCC}} = 110.4^\circ$. The coordinates of the product 2 are $d_{\text{CH}} = 2.416 \text{ Å}$, $\theta_{\text{Me}} \approx 1.0^\circ$, and $\phi_{\text{CCC}} = 112.0^\circ$. The deviation of θ_{Me} from zero is due to numerical inaccuracies.

The initial step in the reaction is a rotation of the methyl group described by θ_{Me} in order to bring the hydrogen atom closer to the phenyl radical. This change in θ_{Me} , while d_{CH} is almost unchanged, is nicely visible in the middle panel of Fig. 2. It causes the shoulder in the energy along the IRC. The energy is further increased by intramolecular distortion expressed in the change in ϕ_{CCC} . From around $\phi_{\text{CCC}} = 110^\circ$ in 1 it is reduced to 103° close to the TS and relaxes back to 112° in 2. This distortion in ϕ_{CCC} is necessary in order to bring the transferred hydrogen atom closer to the phenyl radical. The breaking of the C–H bond finally increases the energy sharply until the TS is reached. After that, the system relaxes directly to 2.

In order to gain more insight into the chemical reaction 1 → 2 we calculated the reaction force, i.e., the negative derivative of the potential energy along the IRC with respect to the path length:^{106,107}

$$F = - \frac{dV(\xi)}{d\xi} \quad (4)$$

The reaction force analysis is an interpretation to distinguish between structural and electronic effects during the course of a chemical reaction¹⁰⁸. This can be achieved by dividing the reaction into three regions which are separated at the extremal points of the reaction force: In the region from the reactant structure

to ξ_1 structural and conformational changes cause an increase of potential energy. In the regions from ξ_1 to ξ_{TS} and from ξ_{TS} to ξ_2 the part of the potential energy barrier caused by electronic effects and the potential energy obtained due to the formation of the new bond can be determined, respectively. In the region from ξ_2 to the product structure, the relaxation of the molecular structure leads to a release of potential energy. The structural and electronic contributions to the activation barrier can be quantized by W_1 and W_2 , and the structural and electronic contributions to the release of energy after passing the transition state can be quantized by W_3 and W_4 , respectively.^{108,109}

$$W_1 = - \int_{\xi_{RS}}^{\xi_1} F(\xi) d\xi \quad W_2 = - \int_{\xi_1}^{\xi_{TS}} F(\xi) d\xi$$

$$W_3 = - \int_{\xi_{TS}}^{\xi_2} F(\xi) d\xi \quad W_4 = - \int_{\xi_2}^{\xi_{PS}} F(\xi) d\xi$$

where ξ_{RS} , ξ_{TS} , and ξ_{PS} are the position of the reactant structure, transition structure, and product structure on the reaction path, respectively. The results can be seen in Fig. 2, second graph, where vertical lines indicate the separation of the three different regions.

In the reaction from **1** to **2** the contribution of the structural changes to the potential energy barrier, W_1 , is higher than the contributions caused by the electronic changes, W_2 , see table 1. The strong structural distortion of the carbon backbone, as can be seen in the change of ϕ_{CCC} close to the transition structure, see Fig. 2, is the source of the huge barrier height. A reduction of this structural stress could therefore lower the potential activation barrier. The impact of this structural change on atom-tunneling though, would then have to be re-evaluated, of course. The structural distortion could be reduced when including a further methylene (CH_2) group leading to the trineopentylphenyl radical. This was already tested by Brunton *et al.*: they reported that the trineopentylphenyl radical was not observed even at -160°C . Thus, they concluded that the following six-membered ring has the optimal spatial arrangement.

The reaction force profile in Fig. 2 shows a minimum at around $\xi = -5.28$ displaying the conformational change, *i.e.*, the rotation of the methyl group.¹¹⁰ After the maximum at $\xi = -3.44$ the structural distortion of the C–C–C angle ϕ_{CCC} takes place. We can therefore separate the work of structural distortion necessary for the reaction, W_1 into the contribution of the methyl rotation and the distortion of the carbon backbone. We call these contributions $W_{1,\text{Me}}$ and $W_{1,\text{struc}}$, see table 1. For the reaction energy, the structural relaxation work, W_4 , is larger than the electronic work. The same trends can be seen, namely

$$|W_3| < |W_4|, \quad (5)$$

indicating that the release of energy due to conformational change is larger than the release of energy due to the formation of the C–H bond.

In summary, the large potential energy barrier stems from structural distortions. Therefore, atom tunneling is facilitated by

structural strain and not, as one could intuitively assume, by a high electronic contribution to the barrier.

Table 1 Structural and electronic contributions during the course of the reaction **1** \rightarrow **2**. W_1 is separated into the structural work caused by the methyl rotation, $W_{1,\text{Me}}$ and the remaining structural distortion of, *e.g.*, the binding angle ϕ_{CCC} . All values in kJ mol^{-1} .

$W_{1,\text{Me}}$	$W_{1,\text{struc}}$	W_2	W_3	W_4
18.3	49.0	11.7	−24.1	−85.0

3.3 Instanton Calculations

The most likely tunneling path, *i.e.*, the instanton, has to be optimized for each temperature. Changes in the mass, as in the calculation of KIEs, also require a re-optimization of the instanton. In principle, for secondary KIEs (KIEs which come from substituting other atoms than the transferred hydrogen atom by their heavier isotopes) the tunneling path can be approximated to remain unchanged.⁵⁵ The spread of the instanton can be interpreted as the delocalization of the individual atoms involved in the chemical process. Lighter atoms tend to be more delocalized. Since the geometrical shape of the instanton qualitatively changes with temperature, we first discuss that before reporting on rate constants.

3.3.1 Tunneling Path

As mentioned above, the instanton path can deviate from the classical reaction path (the IRC), especially at lower temperatures. To aid the discussion, the shapes of the instantons and the IRC are projected onto the two variables d_{CH} and θ_{Me} chosen in the last section, while both IRC and instantons were always obtained by optimizing the full coordinate set.

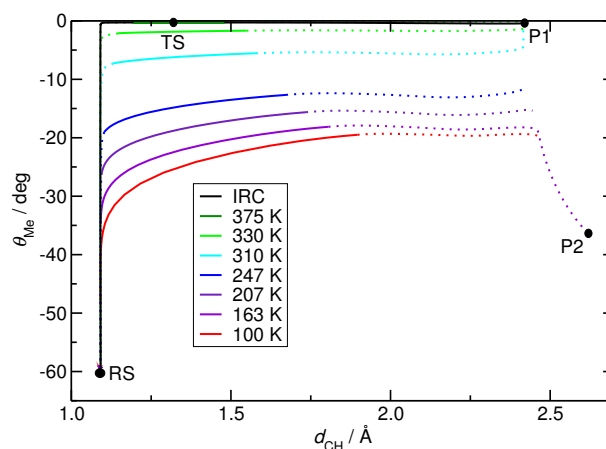


Fig. 5 Shape of instantons and IRC projected onto θ_{Me} and d_{CH} . C_s symmetry corresponds to $\theta_{\text{Me}} = 0^\circ$ and $\theta_{\text{Me}} = 60^\circ$. The dotted lines correspond to steepest-descent paths starting from the instantons' end points.

The IRC per definition starts from the reactant structure (**RS** = minimum-geometry of **1**), proceeds via the **TS** and ends on the product side at **P1**. Both **TS** and **P1** have $\theta_{\text{Me}} = 0^\circ$ and are,

therefore C_s symmetric (*i.e.*, have a mirror plane). **RS** is also C_s symmetric even though $\theta_{Me} = 60^\circ$.

High-temperature instantons are close to the IRC, $\theta_{Me} \approx 0^\circ$. The instanton at 375 K in Fig. 5 therefore coincides with part of the IRC. The instantons are shorter than the IRC, however, because they only connect the points in configuration space, which are located between the classical turning points at a given temperature. Note that the turning points, in general, do not lie on the IRC. We connected them to the minimum geometries in Fig. 5 by calculating the steepest-descent paths in mass-weighted coordinates starting from the endpoints of the instantons using the same algorithm as for calculating the IRC. These connections are shown as dotted lines in Fig. 5.

Below a temperature of 350 K the instantons start to deviate from the C_s symmetry and a qualitative corner cutting effect is found. Similar phenomena were observed for other systems previously.^{19–21,55,63} The continuations by steepest-descent paths connect these instantons to the RS geometry and, for the instantons above 300 K, to the product geometry **P1**. At even lower temperature, the elongation of the tunneling path to the product's side of the barrier ends up in a minimum structure **P2**, which is asymmetric with respect to the methyl rotation angle θ_{Me} .

Both structures **P1** and **P2** were identified as minima by frequency analyses. **P2** is lower than **P1** by 1.5 kJ mol⁻¹. A nudged-elastic band calculation^{111–114} showed a potential energy barrier of merely 0.73 kJ mol⁻¹ between them. It can therefore be assumed that **P1** and **P2** interchange even at temperatures as low as 100 K with a rate much higher than that of $1 \rightarrow 2$.

Here it has to be mentioned that the IRC is strongly curved (see Fig. 5) and the instantons are qualitatively different from the MEP due to corner cutting. At the lowest temperatures presented in this work, the instanton reaction rates even lead to a transition to another minimum structure, which could not have been detected with MEP based tunneling methods. The optimization of the correct tunneling path is therefore necessary for the correct description of the reaction rate constants which will be presented in the following section.

3.3.2 Rate Constants

Rate constants have been calculated for temperatures down to 100 K. Despite the different symmetry along the IRC or instantons, the rotational symmetry numbers σ_i of reactant structure, transition structure and all instantons are equal to one¹¹⁵ and therefore, the reaction's rotational symmetry number $\sigma = 1$. Nevertheless, the rate increases by an additional factor of $\eta = 2$. For the C_1 -symmetric instantons this is caused by their chirality.¹¹⁵ Even for the C_s -symmetric TS, $\eta = 2$ must be applied because it corresponds to the abstraction of just one specific hydrogen atom from the methyl group which is indistinguishable from the hydrogen atom at the other side of the mirror plane in **RS**. At higher temperatures, the methyl group can freely rotate and the factor might be increased to $\eta_{free} = 3$. In the Arrhenius plot in Fig. 6 we used $\eta = 2$ throughout all temperatures.

Accordingly we assume the *tert*-butyl groups and the other individual methyl groups to be hindered in their rotation, too, and treat them as harmonic oscillators. In general the difference of

describing methyl or *tert*-butyl groups as free rotors instead of harmonic oscillators should be minor because the effects in the reactant structure and transition structure cancel. Obviously, the same argumentations are valid for the perdeuterated system.

Rate constants, including those of the perdeuterated system, as well as rate constants without consideration of atom tunneling (calculated by means of harmonic transition state theory) are shown in Fig. 6. A full list of all values is given in the Supplementary Information. We performed a fit of the rate constants to the equation¹¹⁶

$$k(T) = A \exp \left(-\frac{E_0}{R} \frac{T + T_0}{T^2 + T_0^2} \right) \quad (6)$$

which shows good agreement with the instanton values as well as the experimental values. The fit of $k(T)$ allows us to calculate the KIEs, see Fig. 6. The KIE at 100 K is almost 10^6 .

Table 2 Fitting parameters for the hydrogen and deuterium transfer reactions.

	H-transfer	D-transfer
A / s^{-1}	$7.45 \cdot 10^{13}$	$5.25 \cdot 10^{13}$
$E_0 / kJ \text{ mol}^{-1}$	51.51	55.77
T_0 / K	200.2	154.8

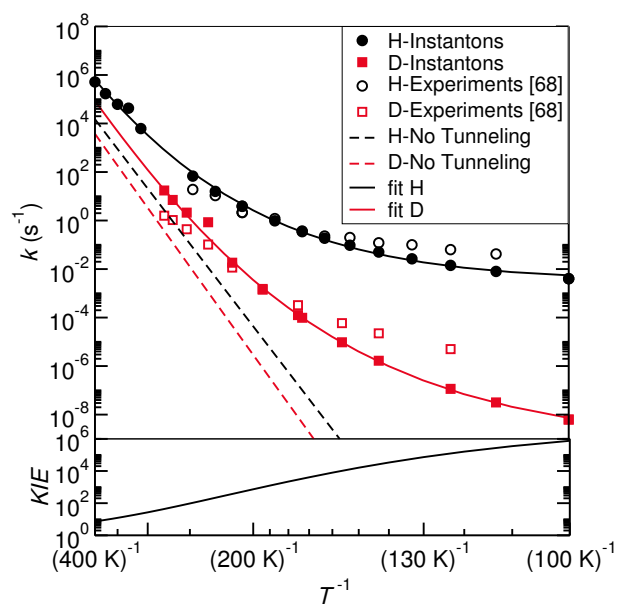
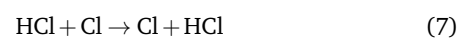


Fig. 6 Arrhenius plot of rate constants obtained with the instanton method compared to the experimental values of reference 68 for the H- and D-transfer reaction.

3.4 Reaction of HCl + Cl

As a complementary example, we want to present the atom transfer reaction



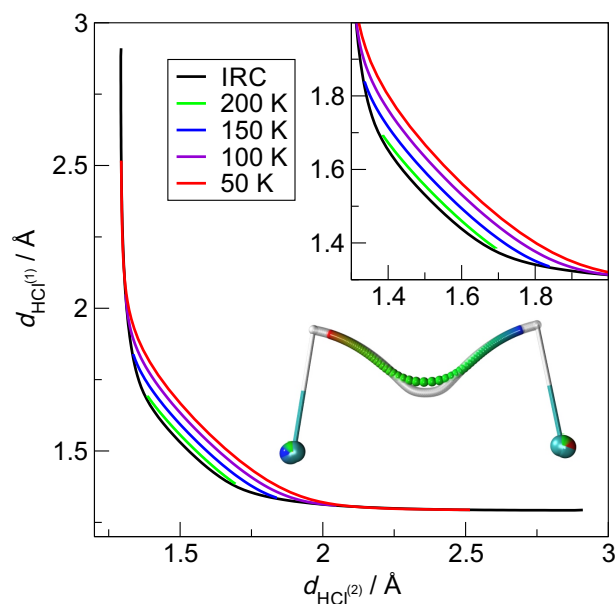


Fig. 7 Corner cutting in the reaction of HCl + Cl: The Cl–H distances are reduced during the tunneling process. At low temperature the corner cutting leads to a significant reduction of the total path length. The picture of the molecular system shows the classical IRC (white path) and the instanton at 50 K (from red to green to blue).

which is an example for a symmetric double-well potential and a prototypic heavy–light–heavy reaction.^{117–121} Thermal rate constants for this reaction can not be observed experimentally except of the reaction with isotopically labelled chlorine. Therefore, we restrict ourselves to the presentation of the instantons and paths.

We calculated the potential energy barrier to be 24.9 kJ mol^{−1}. The barrier is of medium width and the crossover temperature is $T_c = 241.1$ K. We calculated the potential energy along the IRC and instanton paths from 200 K to 35 K. To elucidate the corner cutting effect, one Cl–H distance is plotted against the other Cl–H distance in Fig. 7. As above, high-temperature instantons are closer to the IRC. At lower temperatures, the instantons shorten the distance the hydrogen atom has to cover. For this reaction, the low-temperature instantons are qualitatively of the same shape as the IRC.

The path during a reaction involving atom tunneling can be decomposed into the instanton and the classical steepest-descent paths on the potential energy hypersurface starting from the turning points of the instanton on both sides of the barrier. The instanton path length, the classical path length, and the sum of both are shown in Fig. 8 for different temperatures. At temperatures next to T_c the spread of the instanton is small and the classical path is nearly as long as the full IRC. At lower temperature, the instanton spreads out. The classical path becomes smaller and the sum of both contributions is significantly smaller than the IRC. At 35 K the total tunneling path length is approximately 56.6% of the IRC path length which demonstrates the pronounced corner cutting effect.

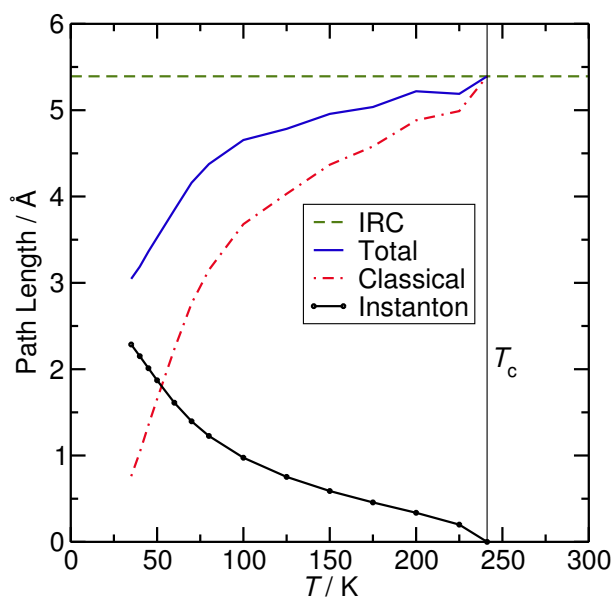


Fig. 8 Contributions of instantons and classical paths to the total path length at various temperatures.

4 Conclusions

In this paper we compare the classical reaction path (IRC) with the tunneling path from semiclassical instanton theory. The instanton, which is the most likely tunneling path at a certain temperature, can deviate qualitatively from the classical reaction path. As examples we used a reaction where a hydrogen atom is transferred from a methyl group to a phenyl radical ($1 \rightarrow 2$) and the reaction of HCl + Cl, which is a prototype for atom tunneling in a heavy–light–heavy arrangement.

For the reaction $1 \rightarrow 2$ experimental data indicated the importance of tunneling.⁶⁸ Instanton theory can reproduce the experimental rate constants within a reasonable accuracy. We performed fits to the instanton rate constants and used these to calculate kinetic isotope effects.

To achieve the comparison, we implemented a modified Hessian predictor-corrector algorithm for the calculation of IRCs. The algorithm uses quadratic information of the potential hyper surface. The scaling is below $\mathcal{O}(N^3)$ because any matrix diagonalizations are avoided. Therefore, it is also suitable for larger systems as long as a single Hessian calculation at the TS can still be carried out.

We have quantified the corner cutting effect by means of a combination of instanton paths and classical paths in the reaction of HCl + Cl.

Acknowledgments

This work was financially supported by the German Research Foundation (DFG) within the Cluster of Excellence in Simulation Technology (EXC 310/2) at the University of Stuttgart. The authors acknowledge support in terms of CPU time by the state of Baden-Württemberg through bwHPC and the Germany Research Foundation (DFG) through grant no INST 40/467-1 FUGG. This work was financially supported by the European Union's Horizon

References

- 1 P. R. Schreiner, H. P. Reisenauer, D. Ley, D. Gerbig, C.-H. Wu and W. D. Allen, *Science*, 2011, **332**, 1300.
- 2 S. Kozuch, *Org. Lett.*, 2014, **16**, 4102–4105.
- 3 S. Kozuch, *Phys. Chem. Chem. Phys.*, 2015, **17**, 16688–16691.
- 4 A. Kohen, *Prog. React. Kinet. Mech.*, 2003, **28**, 119–156.
- 5 J. P. Layfield and S. Hammes-Schiffer, *Chem. Rev.*, 2014, **114**, 3466–3494.
- 6 A. Vardi-Kilshtain, N. Nitoker and D. T. Major, *Arch. Biochem. Biophys.*, 2015, **582**, 18–27.
- 7 T. Hama and N. Watanabe, *Chem. Rev.*, 2013, **113**, 8783–8839.
- 8 S. T. Bromley, T. P. M. Goumans, E. Herbst, A. P. Jones and B. Slater, *Phys. Chem. Chem. Phys.*, 2014, **16**, 18623–18643.
- 9 *Atom Tunneling Phenomena in Physics, Chemistry and Biology*, ed. T. Miyazaki, Springer, Berlin, Germany, 2004.
- 10 J. Kästner, *WIREs Comput. Mol. Sci.*, 2014, **4**, 158.
- 11 J. Meisner and J. Kästner, *Angew. Chem. Int. Ed.*, 2016, **55**, 5400–5413.
- 12 W. T. Borden, *WIREs Comput. Mol. Sci.*, 2016, **6**, 20–46.
- 13 J. Pu, J. Gao and D. G. Truhlar, *Chem. Rev.*, 2006, **106**, 3140–3169.
- 14 G. Nyman, *Int. J. Quant. Chem.*, 2014, **114**, 1183–1198.
- 15 B. M. Garraway and K.-A. Suominen, *Rep. Prog. Phys.*, 1995, **58**, 365.
- 16 R. Marquardt and M. Quack, in *Handbook of High-Resolution Spectroscopy*, Wiley, 2011, ch. Global Analytical Potential Energy Surfaces for High Resolution Molecular Spectroscopy and Reaction Dynamics, pp. 511–549.
- 17 R. P. Bell, *The tunnel effect in chemistry*, Chapman and Hall (London), 1st edn, 1980.
- 18 C. Eckart, *Phys. Rev.*, 1930, **35**, 1303.
- 19 R. A. Marcus and M. E. Coltrin, *J. Chem. Phys.*, 1977, **67**, 2609.
- 20 D. G. Truhlar and B. C. Garrett, *J. Phys. Chem. A*, 2003, **107**, 4006–4007.
- 21 A. Fernandez-Ramos, B. A. Ellingson, B. C. Garrett and D. G. Truhlar, in *Reviews in Computational Chemistry*, John Wiley & Sons, Inc., Hoboken, NJ, USA, 2007, vol. 23, ch. Variational Transition State Theory with Multidimensional Tunneling.
- 22 R. T. Skodje, D. G. Truhlar and B. C. Garrett, *J. Phys. Chem.*, 1981, **85**, 3019–3023.
- 23 J. S. Langer, *Ann. Phys. (N.Y.)*, 1967, **41**, 108.
- 24 J. S. Langer, *Ann. Phys. (N.Y.)*, 1969, **54**, 258–275.
- 25 W. H. Miller, *J. Chem. Phys.*, 1975, **62**, 1899.
- 26 S. Coleman, *Phys. Rev. D*, 1977, **15**, 2929.
- 27 C. G. Callan Jr. and S. Coleman, *Phys. Rev. D*, 1977, **16**, 1762.
- 28 E. Gildener and A. Patrascioiu, *Phys. Rev. D*, 1977, **16**, 423.
- 29 I. Affleck, *Phys. Rev. Lett.*, 1981, **46**, 388–391.
- 30 S. Coleman, *Nucl. Phys. B*, 1988, **298**, 178.
- 31 P. Hänggi, P. Talkner and M. Borkovec, *Rev. Mod. Phys.*, 1990, **62**, 251.
- 32 V. A. Benderskii, D. E. Makarov and C. A. Wight, *Adv. Chem. Phys.*, 1994, **88**, 55.
- 33 M. Messina, G. K. Schenter and B. C. Garrett, *J. Chem. Phys.*, 1995, **103**, 3430.
- 34 J. O. Richardson and S. C. Althorpe, *J. Chem. Phys.*, 2009, **131**, 214106.
- 35 J. O. Richardson and S. C. Althorpe, *J. Chem. Phys.*, 2011, **134**, 054109.
- 36 S. C. Althorpe, *J. Chem. Phys.*, 2011, **134**, 114104.
- 37 J. O. Richardson, *J. Chem. Phys.*, 2016, **144**, 114106.
- 38 S. R. McConnell, A. Löhle and J. Kästner, *J. Chem. Phys.*, 2017, **146**, 074105.
- 39 R. P. Feynman, *Rev. Mod. Phys.*, 1948, **20**, 367.
- 40 S. Chapman, B. C. Garrett and W. H. Miller, *J. Chem. Phys.*, 1975, **63**, 2710.
- 41 G. Mills and H. Jónsson, *Phys. Rev. Lett.*, 1994, **72**, 1124.
- 42 G. Mills, H. Jónsson and G. K. Schenter, *Surf. Sci.*, 1995, **324**, 305–337.
- 43 G. Mills, G. K. Schenter, D. E. Makarov and H. Jónsson, *Chem. Phys. Lett.*, 1997, **278**, 91.
- 44 W. Siebrand, Z. Smedarchina, M. Z. Zgierski and A. Fernández-Ramos, *Int. Rev. Phys. Chem.*, 1999, **18**, 5.
- 45 Z. Smedarchina, W. Siebrand, A. Fernández-Ramos and Q. Cui, *J. Am. Chem. Soc.*, 2003, **125**, 243–251.
- 46 T. Qian, W. Ren, J. Shi, W. E and P. Shen, *Physica A*, 2007, **379**, 491.
- 47 S. Andersson, G. Nyman, A. Arnaldsson, U. Manthe and H. Jónsson, *J. Phys. Chem. A*, 2009, **113**, 4468.
- 48 T. P. M. Goumans and S. Andersson, *Mon. Not. R. Astron. Soc.*, 2010, **406**, 2213–2217.
- 49 T. P. M. Goumans and J. Kästner, *Angew. Chem. Int. Ed.*, 2010, **49**, 7350–7352.
- 50 H. Jónsson, *Proc. Nat. Acad. Sci. U.S.A.*, 2010, **108**, 944–949.
- 51 T. P. M. Goumans, *Mon. Not. R. Astron. Soc.*, 2011, **415**, 3129–3134.
- 52 T. P. M. Goumans, *Mon. Not. R. Astron. Soc.*, 2011, **413**, 26150–2620.
- 53 J. B. Rommel, T. P. M. Goumans and J. Kästner, *J. Chem. Theory Comput.*, 2011, **7**, 690–698.
- 54 J. B. Rommel and J. Kästner, *J. Chem. Phys.*, 2011, **134**, 184107.
- 55 J. Meisner, J. B. Rommel and J. Kästner, *J. Comput. Chem.*, 2011, **32**, 3456–3463.
- 56 T. P. M. Goumans and J. Kästner, *J. Phys. Chem. A*, 2011, **115**, 10767.
- 57 D. M. Einarsdóttir, A. Arnaldsson, F. Óskarsson and H. Jónsson, *Lect. Notes Comput. Sci.*, 2012, **7134**, 45.
- 58 J. B. Rommel, Y. Liu, H.-J. Werner and J. Kästner, *J. Phys. Chem. B*, 2012, **116**, 13682.

- 59 M. Kryvohuz and R. A. Marcus, *J. Chem. Phys.*, 2012, **137**, 134107.
- 60 J. Kästner, *Chem. Eur. J.*, 2013, **19**, 8207–8212.
- 61 S. Álvarez-Barcia, J. R. Flores and J. Kästner, *J. Phys. Chem. A*, 2014, **118**, 78.
- 62 M. Kryvohuz, *J. Phys. Chem. A*, 2014, **118**, 535–544.
- 63 S. Álvarez-Barcia, M.-S. Russ, J. Meisner and J. Kästner, *Faraday Disc.*, 2016, **195**, 69–80.
- 64 L. Song and J. Kästner, *Phys. Chem. Chem. Phys.*, 2016, **18**, 29278–29285.
- 65 T. Lamberts, P. K. Samanta, A. Köhn and J. Kästner, *Phys. Chem. Chem. Phys.*, 2016, **18**, 33021–33030.
- 66 T. Lamberts, G. Fedoseev, J. Kästner, S. Ioppolo and H. Linnartz, *Astron. Astrophys.*, 2017, **599**, A132.
- 67 J. O. Richardson, C. Pérez, S. Lobsiger, A. A. Reid, B. Temelso, G. C. Shields, Z. Kisiel, D. J. Wales, B. H. Pate and S. C. Althorpe, *Science*, 2016, **351**, 1310–1313.
- 68 G. Brunton, D. Griller, L. R. C. Barclay and K. U. Ingold, *J. Am. Chem. Soc.*, 1976, **98**, 6803–6811.
- 69 J. Kästner, J. M. Carr, T. W. Keal, W. Thiel, A. Wander and P. Sherwood, *J. Phys. Chem. A*, 2009, **113**, 11856.
- 70 H. P. Hratchian and H. B. Schlegel, *J. Chem. Phys.*, 2004, **120**, 9918.
- 71 H. P. Hratchian and H. B. Schlegel, *J. Chem. Theory Comput.*, 2005, **1**, 61–69.
- 72 K. Fukui, *Acc. Chem. Res.*, 1981, **14**, 363–368.
- 73 W. Press, *Numerical Recipes in Pascal: The Art of Scientific Computing*, Cambridge University Press, 1989.
- 74 M. Page and J. W. McIver, *J. Chem. Phys.*, 1988, **88**, 922–935.
- 75 M. Page, C. Doubleday and J. W. McIver, *J. Chem. Phys.*, 1990, **93**, 5634–5642.
- 76 H. P. Hratchian, M. J. Frisch and H. B. Schlegel, *J. Chem. Phys.*, 2010, **133**, 224101.
- 77 H. P. Hratchian and M. J. Frisch, *J. Chem. Phys.*, 2011, **134**, 204103.
- 78 P. Dirac, *Proc. Royal Soc. (London) A*, 1929, **123**, 714.
- 79 J. Slater, *Phys. Rev.*, 1951, **81**, 385.
- 80 S. H. Vosko, L. Wilk and M. Nusair, *Can. J. Phys.*, 1980, **58**, 1200–1211.
- 81 A. Becke, *Phys. Rev. A*, 1988, **38**, 3098–3100.
- 82 C. Lee, W. Yang and R. G. Parr, *Phys. Rev. B*, 1988, **37**, 785–789.
- 83 A. D. Becke, *J. Chem. Phys.*, 1993, **98**, 5648.
- 84 F. Weigend and R. Ahlrichs, *Phys. Chem. Chem. Phys.*, 2005, **7**, 3297–3305.
- 85 T. B. Adler, G. Knizia and H.-J. Werner, *J. Chem. Phys.*, 2007, **127**, 221106.
- 86 G. Knizia, T. B. Adler and H.-J. Werner, *J. Chem. Phys.*, 2009, **130**, 054104.
- 87 K. A. Peterson, T. B. Adler and H.-J. Werner, *J. Chem. Phys.*, 2008, **128**, 084102.
- 88 J. Perdew and Y. Wang, *Phys. Rev. B*, 1992, **45**, 13244.
- 89 J. Perdew, K. Burke and M. Ernzerhof, *Phys. Rev. Lett.*, 1996, **77**, 3865.
- 90 J. P. Perdew, M. Ernzerhof and K. Burke, *J. Chem. Phys.*, 1996, **105**, 9982–9985.
- 91 J. P. Perdew, *Phys. Rev. B*, 1986, **33**, 8822–8824.
- 92 A. D. Becke, *J. Chem. Phys.*, 1993, **98**, 1372–1377.
- 93 J. Tao, J. P. Perdew, V. N. Staroverov and G. E. Scuseria, *Phys. Rev. Lett.*, 2003, **91**, 146401.
- 94 V. N. Staroverov, G. E. Scuseria, J. Tao and J. P. Perdew, *J. Chem. Phys.*, 2003, **119**, 12129–12137.
- 95 Y. Zhao and D. G. Truhlar, *Theor. Chem. Acc.*, 2008, **120**, 215–241.
- 96 D. Rappoport and F. Furche, *J. Chem. Phys.*, 2010, **133**, 134105.
- 97 S. Grimme, J. Antony, S. Ehrlich and H. Krieg, *J. Chem. Phys.*, 2010, **132**, 154104.
- 98 H.-J. Werner, P. J. Knowles, G. Knizia, F. R. Manby and M. Schütz, *WIREs Comput. Mol. Sci.*, 2012, **2**, 242–253.
- 99 TURBOMOLE V7.0.1 2015, a development of University of Karlsruhe and Forschungszentrum Karlsruhe GmbH, 1989–2007, TURBOMOLE GmbH, since 2007; available from <http://www.turbomole.com>.
- 100 K. Eichkorn, F. Weigend, O. Treutler and R. Ahlrichs, *Theor. Chem. Acc.*, 1997, **97**, 119–124.
- 101 P. Sherwood, A. H. de Vries, M. F. Guest, G. Schreckenbach, C. R. A. Catlow, S. A. French, A. A. Sokol, S. T. Bromley, W. Thiel, A. J. Turner, S. Billeter, F. Terstegen, S. Thiel, J. Kendrick, S. C. Rogers, J. Casci, M. Watson, F. King, E. Karlsen, M. Sjøvoll, A. Fahmi, A. Schäfer and C. Lennartz, *J. Mol. Struct. (THEOCHEM)*, 2003, **632**, 1.
- 102 S. Metz, J. Kästner, A. A. Sokol, T. W. Keal and P. Sherwood, *WIREs Comput. Mol. Sci.*, 2014, **4**, 101.
- 103 J. M. Bofill, *J. Comput. Chem.*, 1994, **15**, 1–11.
- 104 C. L. Janssen and I. M. Nielsen, *Chem. Phys. Lett.*, 1998, **290**, 423–430.
- 105 N. Lambert, N. Kaltsoyannis, S. D. Price, J. Žabka and Z. Herman, *J. Phys. Chem. A*, 2006, **110**, 2898–2905.
- 106 A. Toro-Labbé, *J. Phys. Chem. A*, 1999, **103**, 4398–4403.
- 107 P. Jaque and A. Toro-Labbé, *J. Phys. Chem. A*, 2000, **104**, 995–1003.
- 108 C. Ortega-Moo, R. Duran, B. Herrera, S. Gutierrez-Oliva, A. Toro-Labbé and R. Vargas, *Phys. Chem. Chem. Phys.*, 2017, **19**, 14512–14519.
- 109 S. Gutiérrez-Oliva, B. Herrera, A. Toro-Labbé and H. Chermette, *J. Phys. Chem. A*, 2005, **109**, 1748–1751.
- 110 D. Yepes, J. S. Murray, P. Politzer and P. Jaque, *Phys. Chem. Chem. Phys.*, 2012, **14**, 11125–11134.
- 111 H. Jónsson, G. Mills and K. W. Jacobsen, in *Classical and Quantum Dynamics in Condensed Phase Simulations*, World Scientific, 1998, ch. Nudged Elastic Band Method for Finding Minimum Energy Paths of Transitions, p. 385.
- 112 G. Henkelman, B. P. Uberuaga and H. Jónsson, *J. Chem. Phys.*, 2000, **113**, 9901.

- 113 G. Henkelman and H. Jónsson, *J. Chem. Phys.*, 2000, **113**, 9978.
- 114 T. P. M. Goumans, C. R. A. Catlow, W. A. Brown, J. Kästner and P. Sherwood, *Phys. Chem. Chem. Phys.*, 2009, **11**, 5431.
- 115 A. Fernández-Ramos, B. A. Ellingson, R. Meana-Pañeda, J. M. C. Marques and D. G. Truhlar, *Theor. Chem. Acc.*, 2007, **118**, 813–826.
- 116 J. Zheng and D. G. Truhlar, *Phys. Chem. Chem. Phys.*, 2010, **12**, 7782–7793.
- 117 M. Kneba and J. Wolfrum, *J. Phys. Chem. A*, 1979, **83**, 69–73.
- 118 Y. Bu, Z. Cao and X. Song, *Int. J. Quant. Chem.*, 1996, **57**, 95–104.
- 119 M. González, J. Hijazo, J. J. Novoa and R. Sayós, *J. Chem. Phys.*, 1998, **108**, 3168–3177.
- 120 G.-Z. Ju and D.-Z. Chen, *Int. J. Quant. Chem.*, 1990, **38**, 75–83.
- 121 C. P. Moradi and G. E. Douberly, *J. Phys. Chem. A*, 2015, **119**, 12028–12035.